Rational design of metal nitride redox materials for solar-driven ammonia synthesis

Ronald Michalsky, Peter H. Pfromm, Aldo Steinfeld

Published Version Information

Citation: Michalsky, M., Pfromm, P. H., & Steinfeld, A. (2015). Rational design of metal nitride redox materials for solar-driven ammonia synthesis. Interface Focus, 5(3), 20140084.

Digital Object Identifier (DOI): doi:10.1098/rsfs.2014.0084

Publisher's Link: http://rsfs.royalsocietypublishing.org/content/5/3/20140084

Rational design of metal nitride redox materials for solar-driven ammonia synthesis

Ronald Michalsky[1, *], Peter H. Pfromm[2], Aldo Steinfeld[1]

[1] Department of Mechanical and Process Engineering, ETH Zürich, 8092 Zürich, Switzerland, [2] Department of Chemical Engineering, 1005 Durland Hall, Kansas State University, Manhattan, KS, 66506, U.S.A.

Abstract

Fixed nitrogen is an essential chemical building block for plant and animal protein, which makes ammonia (NH_3) a central component of synthetic fertilizer for the global production of food and biofuels. A global project on artificial photosynthesis may foster the development of production technologies for renewable NH_3 fertilizer, hydrogen carrier and combustion fuel. This article presents an alternative path for the production of NH_3 from nitrogen, water, and solar energy. The process is based on a thermochemical redox cycle driven by concentrated solar process heat at 700-1200°C that yields NH_3 via the oxidation of a metal nitride with water. The metal nitride is recycled via solar-driven reduction of the oxidized redox material with nitrogen at atmospheric pressure. We employ electronic structure theory for the rational high-throughput design of novel metal nitride redox materials and to show how transition-metal doping controls the formation and consumption of nitrogen vacancies in metal nitrides. We confirm experimentally that iron doping of manganese nitride increases the concentration of nitrogen vacancies compared to no doping. The experiments are rationalized through the average energy of the dopant d-states, a descriptor for the theory-based design of advanced metal nitride redox materials to produce sustainable solar thermochemical ammonia.

Corresponding Author

[*] Present address: ETH Zürich, Institute of Energy Technology, Sonneggstrasse 3, ML K 23, 8092 Zürich, Switzerland; E-mail: michalskyr@ethz.ch; Telephone: +41-44-6338383

Keywords

Concentrated solar energy, Thermochemical redox cycle, Metal nitride, Hydrogen storage, Haber Bosch, Density functional theory

1. Introduction

Renewable chemical fuels, such as hydrocarbons, methanol, hydrogen and ammonia may be synthesized from CO_2, H_2O and N_2 by solar-driven photochemical, [1],[2] electrocatalytic, [3],[4] or thermochemical processes [5]. The latter approach utilizes the entire spectrum of concentrated solar energy as the source of high-temperature process heat, and as such provides a thermodynamically favorable path to solar fuels and materials production with high energy conversion efficiencies. A promising example is the production of syngas by thermochemically splitting CO_2 and H_2O via a metal oxide redox cycle [6] (and references cited therein).

Natural photosynthesis relies on structures – proteins – that are built with fixed nitrogen, such as ammonia (NH_3). Both, sugar, a major product of natural photosynthesis, and protein are the central components of the global food and biofuel production. In turn, synthetic ammonia is one of the major products of the chemical industry [7] that is mainly used as a fertilizer [8]. Additionally, NH_3 is an energy carrier formed via reduction of N_2, analogously to the products of photosynthesis, such as CO and hydrocarbon fuels via reduction of CO_2 and splitting of H_2O. Thus, NH_3 may find application as hydrogen carrier [9],[10] and as a fuel for alkaline fuel cells [11],[12] and in internal combustion engines [13],[14],[15]. Currently, NH_3 is produced industrially from N_2 and H_2 via the catalytic Haber-Bosch process at up to 300 bar and 400-500°C [7],[16],[17],[18],[19]. The overall process is characterized by the high energy consumption associated with the production of the reactants. Usually, H_2 is obtained by steam-reforming of natural gas, while N_2 is obtained by cryogenic separation from air. Both of these processes require a major input of energy, either in the form of heat or electricity, and consequently cause a significant concomitant pollution derived from the combustion of fossil fuels for heat and electricity generation. The total energy requirement is in the range 28-166 GJ/t NH_3 [7],[16]. Furthermore, the severe process conditions require sophisticated high-pressure and high-temperature machinery that is operated in large-scale centralized plants producing typically 1,000-3,000 t NH_3 day^{-1} [7],[18].

To convert the nearly inert N_2 molecule into a reactive chemical, Haber's early studies [20] examined the formation of NH_3 from H_2 and various metal nitrides. These studies were motivated by the temporary formation of NH_3 at low pressures from an iron nitride contamination of the catalyst that Ostwald used [21]. The NH_3 formation ceased quickly since the spent iron nitride could not be regenerated with N_2 at low pressure and the work spurred the development of the

Haber-Bosch process, in which NH_3 is formed at high pressure to shift the thermodynamic equilibrium [20]. Current metal nitrides for the production of complex nitrogen-containing molecules cannot be regenerated with 1 bar N_2 [22]. Examples are Ni_3N, Cu_3N, Zn_3N_2 and Ta_3N_5, which liberate 30, 25, 23, and 13 mol% of their lattice nitrogen in form of NH_3 when reacted with H_2 at 250, 250, 400, and 700°C, respectively [23]. Certain metal nitrides have been studied as low-pressure NH_3 synthesis catalyst [24],[25] and some ternary metal nitrides have been found to reversibly reduce N_2 at low pressure and to liberate the fixed nitrogen in form of NH_3 in a second step, when reacted with H_2 [26],[27],[28]. A typical example of such a material is Co_3Mo_3N that yields Co_6Mo_6N and up to 8 mol% of its lattice nitrogen in form of NH_3 when reacted for 60 min with H_2 at 400°C [28]. To increase the NH_3 yield, current materials development focuses on increasing the amount of nitrogen stored in the metal nitride and on increasing the fraction of the lattice nitrogen that yields NH_3 [22].

This paper focuses on materials development for a solar-driven ammonia synthesis from N_2 and H_2O (instead of H_2) that – in contrast to the Haber-Bosch process – does not require fossil fuels, electricity, or high-pressure operations [29],[30],[31]. In a first step, NH_3 is formed at 1 bar and below 200-500°C via the oxidation of a solid metal nitride redox material with steam [32],[33]. The oxidized redox material is subsequently regenerated in an endothermic step driven by concentrated solar process heat at up to 1200°C with a stream of N_2 with or without a gaseous chemical reducing agent [29],[30],[31]. The reaction stoichiometry of this redox cycle is given with Supporting Information (SI). While this process has been demonstrated successfully with Al-based redox materials, [34],[35],[36] the fixation of N_2 with Al_2O_3 requires a carbonaceous reducing agent and technically-challenging temperatures above 1700°C. [30],[36],[37]. Certain transition-metal redox materials such as Cr-based nitrides have been shown to circumvent the need for a solid reducing agent and allow to regenerate the nitride below 1500°C, but at the expense of lower extents of the nitrogen fixation and ammonia evolution [29],[30],[31].

Only few metals accomplish the trade-off between thermodynamically stable formation of a metal nitride from N_2 that gives NH_3 upon hydrolysis [30],[32],[33] and formation of only intermediately stable metal oxides that can be recycled at moderate process conditions [29],[30]. This is in analogy to the Sabatier principle in heterogeneous catalysis [38] that describes the ideal catalytic activity of a material as function of an intermediately strong bond formed between the catalyst surface and key reaction-intermediates [19],[25]. As a starting point, we have chosen Mo and Mn as primary metals for the development of advanced metal nitride redox materials.

However, while both metals exhibit promising characteristics, Mo binds nitrogen slightly too weak leading to relatively low nitride and NH_3 yields [30],[32] and Mn binds nitrogen somewhat too strong leading to the formation of relatively stable metal oxides due to the correlated stability of metal nitrides and metal oxides [39].

Here, we employ electronic structure computations to show how the bonding of nitrogen in the solid state can be controlled via doping with transition metals. Such novel theory-assisted design is analogous to the rational design of metal oxide redox materials [40],[41],[42], where reactivity is controlled by the oxygen vacancy formation energy [40],[41]. To verify the concept, we experimentally demonstrate controlling nitrogen vacancy formation in manganese based redox materials. Finally, we rationalize the trends in the Gibbs free energy of the nitrogen vacancy formation with the charge density distribution in the ternary metal nitrides and the d-band center, a quantitative descriptor for the theory-based design of advanced metal nitride redox materials for sustainable solar-derived ammonia.

This work is at the interface of fundamental physical science of redox materials on one hand, and chemical engineering to store solar energy as ammonia. The ultimate vision of this work is a device that converts nitrogen from air, water and sunlight, at ambient pressure and without electricity, into ammonia and oxygen. Such a device would facilitate the production of NH_3 fuel, as an alternative to carbon-based fuels derived from solar-driven CO_2 and H_2O splitting. Ammonia fertilizer for food and biofuels could be produced without the infrastructure for supplying natural gas or coal and the know-how and technology for the high-pressure operations employed globally for the production of synthetic NH_3. A global project on artificial photosynthesis, as it is contemplated in this themed issue, [43],[44] could raise the public profile of this field and may assist in funding the development of solar-derived NH_3 through governmental, private, and corporate contributions. Although solar-derived NH_3 may be economically more attractive in certain geographically, economically, or politically isolated regions than NH_3 from large-scale Haber-Bosch plants, accounting for ethical implications, such as diminished environmental impacts when avoiding the dependence on fossil fuel feedstock, may make solar-derived NH_3 economically competitive with NH_3 from Haber-Bosch plants. In this sense, solar-driven N_2 reduction is equivalent to solar-driven CO_2 reduction and H_2O splitting, the central reactions of “synthetic photosynthesis” for an efficient production of solar fuel and food as well as acquisition of knowledge: Ethically, they are common heritage of humanity and should not be fully owned by profit-focused private interests. The mild process

conditions of solar-derived ammonia will allow implementation in parts of the world that may lack the infrastructure for a highly complex high pressure catalytic process like the Haber-Bosch based approach to ammonia. Ideally, global synthetic photosynthesis should he held on trust for humanity and its ecosystems and should be employed through a politically and economically neutral agency [44]. As verbalized at the Royal Society's meeting discussing a global artificial photosynthesis project at Chicheley Hall in 2014: "Our goal is to work cooperatively and with respect for basic ethical principles to produce the scientific breakthroughs that allow development and deployment of an affordable, equitably accessed, economically and environmentally sustainable, non-polluting global energy and food system that also contributes positively to our biosphere."

2. Methods and Materials

2.1 Thermochemical equilibrium calculations

To quantify the potential of binary transition-metal nitride redox materials for a solar-driven ammonia synthesis, the thermochemical equilibrium of the redox cycle was analyzed for Mo- and Mn-based bulk metal nitrides at 1 bar and as a function of temperature from tabulated free energy data [39]. We note negative free energy differences mark exergonic reactions.

2.2 Electronic structure calculations

To quantify the effect of doping on the nitrogen vacancy formation energetics in transition-metal nitrides, cubic γ-Mo_2N and hexagonal ζ-Mn_2N were modeled via density functional theory (DFT), performed with the Grid-based projector-augmented wave (GPAW) code [45],[46]. Exchange-correlation interactions were treated by the revised Perdew-Burke-Ernzerhof (RPBE) functional of Hammer, Hansen, and Nørskov [47] and atomic configurations were handled in the Atomic Simulation Environment (ASE) [48],[49]. Mo_2N and Mn_2N were modeled with four and eight metal atoms, respectively, and the stoichiometric amount of nitrogen occupying half of the octahedral interstitial sites. The bulk structures had periodic boundary conditions in all directions and were modeled with a **k**-point sampling of 4×4×4. The corresponding $D_{0.5}Mo_{1.5}N$ and $D_{0.25}Mn_{1.75}N$ ternary metal nitride models were created via replacing one of the parent metal atoms in each model with a dopant, D = Sc, Ti, V, Cr, Mo, Mn, Fe, Co, Ni, Cu or Zn, where all compositions containing Mn, Fe, Co, or Ni were modeled with spin-polarized calculations. The free energy of forming nitrogen vacancies in the bulk was determined as the difference in the total electronic energy of the metal nitride with nitrogen vacancies (50% and 25% relative to the

stoichiometric composition of Mo_2N and Mn_2N, respectively) and the stoichiometric metal nitride plus the chemical potential of N_2 in the gas phase. The value was converted to free energy at 25°C and 1 bar using standard statistical mechanical equations evaluated through ASE. The partial charge density was determined for all metal nitride models via Bader decomposition [50]. Computational details are given with SI.

2.3 N_2 reduction

The effect of doping Mo- and Mn-based redox materials with Cr and Fe on the stability of the metal nitrides formed by Mo and Mn, respectively, was studied by reacting approximately 0.75-2.00 g Cr, Mn, Fe, Mo, or equimolar Mo/Cr and Mn/Fe metal powder mixtures with N_2. The metal powder was placed into a quartz boat and heated with a tube furnace (HTF55347C furnace, CC58434C temperature controller, Lindberg/Blue) for 0.5, 5, 10, 30, and 120 min (all samples) and 60, 90, and 240 min (samples containing Mn) at 750°C in 1.86 $L_{(STP)}N_2$ min^{-1} (all samples) and 1.86 $L_{(STP)}N_2$ min^{-1} diluted with 0.47 $L_{(STP)}H_2$ min^{-1} (samples containing Mo or Cr). All metals (99.8% pure Cr, 99.9% Mn, 99.9% Fe, and 99.95% Mo, from Noah Technologies, minor impurity levels are specified with SI) were -325 mesh and had comparable average particle diameters and specific BET surface areas, as shown with SI. All gases were of UHP Zero grade (Linweld). This article discusses the data for the N_2 reduction with Mn, Fe, and Mn/Fe, while the data for Mo, Cr, and Mo/Cr is given with SI.

2.4 Solid-state analysis

The composition of the solids was quantified via powder X-ray diffraction (XRD) using a Miniflex II diffractometer (5-80 °2θ range, Cu-target X-ray tube, 30 kV / 15 mA output, diffracted beam monochromator, Rigaku). Scanning electron microscopy (SEM) was used (S-3500N Scanning Electron Microscope, Hitachi, 20 kV) to determine the average particle diameter and energy-dispersive X-ray spectroscopy (EDS, Nova NanoSEM 430, FEI Company, 5-15 kV, beam deceleration, high stability Schottky field emission gun, and Oxford X-Max Large Area Analytical silicon drift detector) was used to map the distribution of metal dopant and nitrogen at the surface. All reactants and products were weighed (AE260 DeltaRange balance, Mettler) and the specific BET surface area was analyzed by NanoScale Inc., Manhattan, KS.

3. Results and Discussion

3.1 Controlling the nitrogen vacancy formation in transition-metal nitrides

To drive a two-step ammonia synthesis with concentrated solar energy and to facilitate the use of water as hydrogen source for the NH_3 evolution, this section outlines the process conditions of a solar-thermochemical ammonia synthesis with metal nitride redox materials. We start our analysis with thermochemical equilibrium calculations for Mn_5N_2 and Mo_2N, metal nitrides that facilitate the trade-off between high NH_3 yields on one side and high N_2 reduction yields on the other side. Thereafter we establish a rationale for how to further improve this trade-off via doping metal nitrides with transition metals.

Figure 1A shows the thermodynamic equilibrium for the oxidation of Mn_5N_2 with water at 1 bar yielding MnO, NH_3 and the balance H_2. As indicated with the shaded area, the reaction is exergonic – that is thermodynamically favoring the formation of the reaction products – over the entire examined temperature range. We note forming NH_3 at elevated temperatures and 1 bar requires the need to quickly remove NH_3 from the reactor to thereby avoid its decomposition into N_2 and H_2 above 180°C at thermodynamic equilibrium [20],[30]. The oxygen can be abstracted from the formed MnO in a second step above 1230°C (below the melting point of Mn) using by-produced H_2 as reducing agent and ensuring that the partial pressure of water, pH_2O, is below 1.5×10^{-4} bar. This endothermic reaction can be driven with concentrated solar radiation and stores the chemical potential in the redox material that is employed for the subsequent reduction of N_2 at 1 bar yielding Mn_5N_2 below 1060°C. **Figure 1B** shows that the composition of the metal nitride allows to alter these reaction conditions: with Mo_2N the NH_3 evolution and the N_2 reduction are both limited at 1 bar to temperatures below 640°C and 700°C, respectively. However, the reduction of the formed MoO_2 can be achieved more facile with CO as reducing agent (e.g., from gasified biomass) at above 730°C and below 4.0×10^{-1} bar pCO_2. We note the ideal temperature for the reduction of MoO_2 with CO depends also on the vapor pressure of the molybdenum oxides that are formed during the NH_3 evolution and the tendency for undesirable carbon deposition in the reactor.

The ideal metal nitride composition would confer thermochemical properties to the redox material for a solar-driven NH_3 synthesis that lie between those of Mn_5N_2 and Mo_2N. Ideally, the metal nitride should be slightly more stable than Mo_2N – to fix more nitrogen above 700°C – while the metal oxide should be less stable than MnO – to avoid the need for temperatures above

1200°C and the means to establish low partial pressures of H_2O or CO_2, respectively. Similar to the possibility to control the adsorption energy of adsorbates at surfaces by altering the surface composition, [19],[19],[25],[38] doping bulk metal nitrides with transition metals may diminish or augment the formation of the metal nitride [51]. However, no rationale exists yet that describes how to compose metal nitrides to control the stability of the lattice nitrogen.

To establish trends in the effect of doping transition-metal nitrides on the bonding of the lattice nitrogen, we compute the free energy of the nitrogen vacancy formation across 22 metal nitride compositions. We hypothesize, negative free energies of the nitrogen vacancy formation correlate with metal nitride compositions that spontaneously liberate lattice nitrogen (in from of NH_3 if a hydrogen source such as H_2 or H_2O is present) and that less readily form lattice nitrogen from N_2, and vice versa. **Figure 2** plots the free energy of the nitrogen vacancy formation in Mn_2N bulk (i.e., the ζ-phase manganese nitride with a broad stoichiometry that includes Mn_5N_2 and $Mn_6N_{2.58}$) [52] doped with a 3d transition metal or Mo vs. the number of d-electrons in the ground state of the dopant. The figure shows that all tested dopants decrease the stability of the lattice nitrogen, relative to the value for un-doped Mn_2N, which is shown with a solid line. As a general trend, a high occupancy of the dopant d-states correlates with a high un-stability of the lattice nitrogen. In other words, filling the metal d-states of the metal nitride decreases the bonding strength of the lattice nitrogen. We note $Zn_{0.25}Mn_{1.75}N$ shows the largest deviation from this trend, which is discussed in Section 3.3. **Figure 3** shows the equivalent analysis for Mo_2N. The steeper slope of the linear correlation for Mo_2N, i.e., -0.162 eV for Mo_2N vs. -0.072 eV for Mn_2N, suggests that the stability of the lattice nitrogen in doped Mo_2N is significantly more sensitive to the occupancy of the d-states than the stability of the lattice nitrogen in doped Mn_2N. In summary, the formation and consumption of nitrogen vacancies in transition-metal nitrides can be controlled with the occupancy of the metal d-states. Aiming at the design of metal nitride redox materials, we suggest the relative strong binding of nitrogen in Mn_2N may be diminished via doping with metals such as Fe while the relative weak binding of nitrogen in Mo_2N may be augmented via doping with metals such as Cr.

3.2 N_2 reduction with Fe-doped Mn

The test the predicted weakening of the nitrogen bonding in manganese nitride when doping with late transition metals, this section evaluates trends in the formation of manganese nitrides and iron nitrides from manganese, iron, an equimolar mixture of both metals and N_2 at 1 bar and

750°C. **Figure 4A** shows the formation of ε-Mn_4N and ζ-$Mn_6N_{2.58}$ (which is equivalent to Mn_5N_2 and Mn_2N discussed in Section 3.1) [52] as a function of time. Mn fixes N_2 quickly, yielding about 85 mol% Mn_4N after 30 min. Thereafter, the yield of Mn_4N decreases while the yield of the additional $Mn_6N_{2.58}$ phase increases to 85 mol% $Mn_6N_{2.58}$ after 240 min, indicating that the nitride with increased nitrogen content is formed via nitridation of the nitride with lower nitrogen content. We note the formation of these two manganese nitride phases is as predicted by the Mn-N phase diagram, [53] while the η and θ phases with higher nitrogen content [52] are unstable at 750°C [53]. Furthermore, the transformation of the ε phase via nitridation into the ζ phase is expected [53] and analogous to the formation of related interstitial nitrides, such as CrN from Cr_2N [29]. Details on the crystal phases and physical characteristics of the redox materials are given with Table S1 (SI). In the presence of Fe, as shown with **Figure 4B**, the quick formation of Mn_4N levels after 30 min at approximately 64 mol% and the subsequent formation of $Mn_6N_{2.58}$ reaches only 29 mol% after 240 min. That is, Mn fixes about 0.24-0.28 mol nitrogen per mol Mn after 60-240 min in the presence of Fe, which is about 66-74% of 0.32-0.40 mol nitrogen fixed per mol Mn in the absence of Fe. This indicates that Fe destabilizes the lattice nitrogen in manganese nitrides. Assessing whether or not the dopant affects the diffusion kinetics of the nitrogen vacancies as well requires further studies.

While Fe appears to destabilize the bond that is formed between Mn and the lattice nitrogen, Mn stabilizes the formation iron nitrides that are thermodynamically unstable in the absence of Mn, as shown with **Figure 5**. As expected, [39] Fe does not reduce N_2 at 1 bar and 750°C. However, in the presence of Mn some nitrogen appears to intercalate into the Fe lattice yielding up to 54 mol% of a cubic $FeN_{0.0324}$ phase after 240 min. In conclusion, iron appears to diminish the formation of manganese nitrides – as predicted with Figure 2 – while manganese augments the formation of iron nitrides – in agreement with the lower occupancy of the d-states in Mn vs. Fe, as discussed in Section 3.1.

We note while the preparation and cycling of ternary metal nitrides [26],[27],[28] or nano-composites would provide the possibility to quantify the effect of the dopant on the bond energy of the lattice nitrogen, the discussed data for metal powders and metal powder mixtures confirms the trends in the stability of transition-metal nitrides predicted via electronic structure theory. To visualize the morphology of the metal nitrides employed in this work, **Figure 6** shows SEM images of cubic Mn_4N (up to 84.6 mol%), mostly cubic Mo and tetragonal Mo_2N (up to 21.1

mol%) and a powder mixture of mostly trigonal Cr_2N, cubic Mo and some cubic CrN and tetragonal Mo_2N. Details are given with SI. The X-ray emission map of the metal powder mixture shows that the parent metal, Mo, and the metal dopant, Cr, are closely located in some regions. We suggest that these are the domains where the bonding of the lattice nitrogen is affected by both metals, while in other domains of the metal mixture the bonding of nitrogen is dominated by the presence of one metal only. We note while Cr increases the fraction of nitrogen fixed by Mo, as shown with Figure S2 (SI), the amount of nitrogen fixed by Mo is still below that fixed by Cr, as shown in Figure 6C by the inhomogeneous distribution of nitrogen mostly located with Cr. The Cr dopant appears to support the nitridation of Mo with N_2 into Mo_2N, presumably due to reduction of molybdenum oxides at the surface (discussed with SI) and due to stronger binding of the lattice nitrogen (such as discussed above for the formation of iron nitrides).

From a practical perspective, an optimized metal nitride redox material should provide a high specific surface area for the formation and consumption of nitrogen vacancies, either via a porous structure [54], similar to the structure of advanced metal oxide redox materials [55], or in form of a porous particle bed [56]. As a starting point we have computed the apparent nitrogen diffusion constants at 750°C (see details in the SI) with 7.77×10^{-9} cm^2 s^{-1} for the formation of $Mn_6N_{2.58}$ and 3.07×10^{-11} cm^2 s^{-1} for the formation of Mo_2N. These values compare well with those reported previously, i.e., 3.07×10^{-9} cm^2 s^{-1} for the ζ-manganese nitride phase at 890°C [57] and 5×10^{-9} to 3×10^{-14} cm^2 s^{-1} for Mo_2N at 600-750°C [58],[59]. Comparing these values for a presumably interstitial nitrogen diffusion process [58] to the diffusion constants for nitrogen vacancy diffusion in good anion conductors, such as 2×10^{-11} cm^2 s^{-1} at 700°C in nitrogen-doped yttria-stabilized zirconia, [60] indicates that transition-metal nitrides are promising materials for the fixation of N_2 [58]. Due to the higher fraction of fixed nitrogen per metal and the higher diffusion constant, manganese nitrides might be ideal starting materials for the development of advanced metal nitride redox materials for a solar-driven low-pressure ammonia synthesis.

3.3 Electronic structure descriptors

To understand how doping controls the formation and consumption of nitrogen vacancies in transition-metal nitrides, this section discusses trends in the electronic structure of doped Mn_2N and doped Mo_2N. We find that the stability of the lattice nitrogen in these materials can be predicted with the average energy of the metal d-states of the dopant and the quantity and

geometry of partially localized electronic charge. Employing these trends for the computational screening [3],[61] of advanced metal nitride redox materials is outlined.

Figure 7A decomposes the electronic interaction of the metal dopant, as an example for doped Mo_2N, into the metal-projected s-, p-, and d-orbitals. The figure identifies continuous filling of the d-states and emptying of s- and p-states when moving the dopant from the left to the right in the periodic table. These trends correlate with a decreasing stability of the lattice nitrogen, as shown with **Figure 7B** and **7C**. Figure 7B employs the b-band center – that is the central moment of the dopant d-band – as a descriptor for the electronic structure trends in transition-metal doped metal nitrides. This metric has been used successfully for describing adsorption energy trends at transition-metal surfaces which, in turn, has revolutionized the high-throughput screening of advanced catalysts [62]. As a general trend, the positive slope of the correlation shown with Figure 7B identifies the anti-bonding character of the dopant d-states, while the negative slope of the two correlations shown with Figure 7C identifies the bonding contribution of the dopant s- and p-states to the bonding of the lattice nitrogen. However, while the d-band center yields a linear correlation with predictive value, the correlation of the p- and, in particular, the s-band center is rather qualitative. Essentially, only the values for the Zn dopant deviate from the d-band center correlation which can be understood due to the stable configuration of the completely filled Zn d-states, as discussed with SI.

To understand the difference in the sensitivity of the scaling between the free energy of the nitrogen vacancy formation and the number of electrons in the dopant d-states, which is shown with Figure 2 and 3, we compute the partial charge localized at the metals and nitrogen in the metal nitride models. **Figure 8A** and **8B** show the correlation of the free energy of the nitrogen vacancy formation with the partial charge localized at the dopant and the partial charge localized in average at the lattice nitrogen, respectively. Generally, a high amount of net-positive charge localized at the dopant and a high amount of net-negative charge localized at the lattice nitrogen correlate with stable lattice nitrogen. The steeper slope of scaling of the free energy of the nitrogen vacancy formation with the partial dopant charge for $D_{0.5}Mo_{1.5}N$ vs. $D_{0.25}Mn_{1.75}N$ suggests that the dopant donates nearly the same amount of charge in both materials which, however, has a stronger effect on the bonding of the lattice nitrogen in $D_{0.5}Mo_{1.5}N$ relative to $D_{0.25}Mn_{1.75}N$. The larger increase or decrease of charge density at the lattice nitrogen when doping $D_{0.5}Mo_{1.5}N$ vs. $D_{0.25}Mn_{1.75}N$, shown with Figure 8B, can therefore be understood due to the dopant concentration in the metal nitride. Doping Mo_2N with twice the amount of metal,

compared to Mn_2N, yields nearly twice the amount of charge density change in average at the lattice nitrogen, relative to the un-doped metal nitride. Previous studies have suggested that the bonding of nitrogen in metal nitrides can be controlled via metal doping [51]. The trends discussed here indicate that the stability of the lattice nitrogen in transition-metal nitrides can be controlled with the type and the amount of a metal dopant due to the anti-bonding character of the dopant d-states as well as due to the amount of charge density transferred to the lattice nitrogen.

Comparable to the trends in the quantity of the charge density transfer, forming nitrogen vacancies in ternary metal nitrides shows also trends in the geometry of the charge distribution. **Figure 9A** analyzes changes in the charge density due to the formation of nitrogen vacancies in Mo_2N. Darker shaded areas mark regions with accumulated charge (charge sinks) while lighter areas mark regions from which charge is withdrawn (charge sources). As shown schematically with **Figure 9B**, the stability trends of the lattice nitrogen can be understood due to attractive and repulsive electronic interactions between charge density sinks and sources.

In detail, doping Mo_2N with Sc or Ti results in stronger binding of the lattice nitrogen compared to no doping, as shown with Figure 3. For these dopants, the charge density difference near the dopant exhibits four 3d lobes that are nearly equally pronounced. For the V, Cr and Mo dopants, the binding of the lattice nitrogen decreases while the charge density starts to accumulate at the dopant, next to the lattice nitrogen. When doping with Mn, Fe, Co, and Ni the binding of the lattice nitrogen decreases further while charge density also accumulates at the lattice nitrogen. This suggests that the weaker binding of the lattice nitrogen is due electronic repulsion between two charge sinks. This also explains why the binding of the lattice nitrogen does not decrease further when further increasing the occupancy of the dopant d-states, i.e., when doping with Cu and Zn. For the Cu dopant the spatial polarization of the charge density difference at the dopant weakens while it nearly changes its polarization for the Zn dopant, which appears to cancel the repulsion between two charge sinks. This correlates with an increase in the stability of the lattice nitrogen in Mo_2N when doping with Zn. Further details of this analysis are given with SI that is showing the charge density differences due to doping in Mn_2N.

4. Conclusions

Complementing the production of solar fuels and chemicals via synthetic photosynthesis, NH_3 fertilizer from solar-driven N_2 and H_2O splitting could aid in the global and decentralized production of solar-derived food and biofuels. Renewable NH_3 fuel might be an attractive

alternative to carbon-based fuels derived from solar-powered CO_2 and H_2O splitting, the central reactions of synthetic photosynthesis. In this sense, this work contributes with novel design principles for metal nitride redox materials to the development of a global project on artificial photosynthesis which, in turn, could raise the public profile of this field and may assist in funding the development of solar ammonia production.

Here we have outlined the process conditions required to produce NH_3 from H_2O and N_2 with a metal nitride redox material and concentrated solar radiation at ambient pressure. This can be achieved with Mo_2N that is oxidized with H_2O at approximately 500°C and recycled from the formed MoO_2 with N_2/CO at 750°C and below 4.0×10^{-1} bar pCO_2. As an alternative, NH_3 can be formed with Mn_5N_2 that is oxidized with H_2O at or above 500°C and recycled from the formed MnO with N_2/H_2 at 1000-1230°C and below 1.5×10^{-4} bar pH_2O. Due to the intermediate thermochemical stability of Mn_5N_2 and MnO, the fast formation kinetics of Mn_4N, and relative fast apparent solid-state diffusion of nitrogen in $Mn_6N_{2.58}$, manganese nitride was identified as an ideal candidate for the development of ternary metal nitride redox materials. To further decrease the correlated stability of the metal oxide, the design of ternary manganese-based metal nitrides focuses on destabilizing the lattice nitrogen. We have employed electronic structure theory to show that the stability of the lattice nitrogen in transition metal nitrides can be increased or decreased to a desirable process- and redox material-dependent value via doping with transition metals. This was verified experimentally for manganese nitride doped with iron. The electronic structure trends of transition-metal nitrides suggest that the nitrogen bonding is destabilized with an increasing occupancy of the anti-bonding dopant d-states. The d-band center has been identified as a quantitative descriptor that can be computed from first principles and utilized for the high-throughput screening of advanced metal nitrides for a solar-driven NH_3 synthesis at moderate process conditions.

Acknowledgments

We gratefully acknowledge the financial support by the European Research Council under the European Union's ERC Advanced Grant (SUNFUELS — No. 320541), the Swiss Competence Center Energy & Mobility, the US National Science Foundation Grant # 0903701 (Integrating the Socioeconomic, Technical, and Agricultural Aspects of Renewable and Sustainable Biorefining Program), and the Center for Sustainable Energy at Kansas State University. We thank Alexandru M. Avram, Daniel L. Boyle, Kent E. Hampton, and James R. Hodgson for their technical

assistance. Experimentation was carried out at Kansas State University. The theoretical calculations and analyses were conducted at the High-Performance Computation cluster of ETH Zürich.

Electronic supplementary material

Computational and experimental details, N_2 reduction yields and kinetics with Mo, Cr and Cr-doped Mo at 1 bar, 450-1200°C and 0-120 min, comprehensive summary of the N_2 reduction rate constants, diffusion constants, complete Bader charge analysis and DOS plots for the dopant-projected d-states, Charge density differences due to doping in Mn_2N, Data repository.

References

1. Valdés, A., et al. 2012 Solar hydrogen production with semiconductor metal oxides: new directions in experiment and theory. Physical Chemistry Chemical Physics 14, 49-70.
2. Lewis, N. S., Nocera, D. G. 2006 Powering the planet: Chemical challenges in solar energy utilization. Proceedings of the National Academy of Sciences of the United States of America 103, 15729-15735.
3. Peterson, A. A., Nørskov, J. K. 2012 Activity Descriptors for CO_2 Electroreduction to Methane on Transition-Metal Catalysts. Journal of Physical Chemistry Letters 3, 251-258.
4. Amar, I. A., Lan, R., Petit, C. T. G., Tao, S. 2011 Solid-state electrochemical synthesis of ammonia: a review. Journal of Solid State Electrochemistry 15, 1845-1860.
5. Romero, M., Steinfeld, A. 2012 Concentrating solar thermal power and thermochemical fuels. Energy & Environmental Science 5, 9234-9245.
6. Smestad, G. P., Steinfeld, A. 2012 Review: Photochemical and thermochemical production of solar fuels from H_2O and CO_2 using metal oxide catalysts. Industrial & Engineering Chemistry Research 51, 11828-11840.
7. Rafiqul, I., Weber, C., Lehmann, B., Voss, A. 2005 Energy efficiency improvements in ammonia production - perspectives and uncertainties. Energy 30, 2487-2504.
8. Smil, V. 1999 Detonator of the population explosion. Nature 400, 415-415.
9. Klerke, A., Christensen, C. H., Nørskov, J. K., Vegge, T. 2008 Ammonia for hydrogen storage: Challenges and opportunities. Journal of Materials Chemistry 18, 2304-2310.
10. Christensen, C. H., Johannessen, T., Sørensen, R. Z., Nørskov, J. K. 2006 Towards an ammonia-mediated hydrogen economy? Catalysis Today 111, 140-144.

11. Vitse, F., Cooper, M., Botte, G. G. 2005 On the use of ammonia electrolysis for hydrogen production. Journal of Power Sources 142, 18-26.
12. Ganley, J. C. 2008 An intermediate-temperature direct ammonia fuel cell with a molten alkaline hydroxide electrolyte. Journal of Power Sources 178, 44-47.
13. Gross, C. W., Kong, S. C. 2013 Performance characteristics of a compression-ignition engine using direct-injection ammonia-DME mixtures. Fuel 103, 1069-1079.
14. Ryu, K., Zacharakis-Jutz, G. E., Kong, S. C. 2014 Performance enhancement of ammonia-fueled engine by using dissociation catalyst for hydrogen generation. International Journal of Hydrogen Energy 39, 2390-2398.
15. http://nh3fuelassociation.org/2013/06/20/the-amveh-an-ammonia-fueled-car-from-south-korea/ (retrieved 5/2/14).
16. Kirova-Yordanova, Z. 2004 Exergy analysis of industrial ammonia synthesis. Energy 29, 2373-2384.
17. Ertl, G. 2008 Reactions at surfaces: From atoms to complexity (Nobel lecture). Angewandte Chemie-International Edition 47, 3524-3535.
18. Hellman, A., et al. 2006 Predicting catalysis: Understanding ammonia synthesis from first-principles calculations. Journal of Physical Chemistry B 110, 17719-17735.
19. Jacobsen, C. J. H., Dahl, S., Clausen, B. S., Bahn, S., Logadottir, A., Nørskov, J. K. 2001 Catalyst design by interpolation in the periodic table: Bimetallic ammonia synthesis catalysts. Journal of the American Chemical Society 123, 8404-8405.
20. Haber, F., van Oordt, G. 1905 Über die Bildung von Ammoniak aus den Elementen. Zeitschrift für anorganische Chemie 44, 341-378.
21. Hager, T. 2008 The Alchemy of Air: A Jewish Genius, a Doomed Tycoon, and the Scientific Discovery That Fed the World but Fueled the Rise of Hitler. Three Rivers Press, New York.
22. Hargreaves, J. S. J. 2014 Nitrides as ammonia synthesis catalysts and as potential nitrogen transfer reagents. Appl Petrochem Res 4, 3-10.
23. Alexander, A. M., Hargreaves, J. S. J., Mitchell, C. 2012 The reduction of various nitrides under hydrogen: Ni_3N, Cu_3N, Zn_3N_2 and Ta_3N_5. Topics in Catalysis 55, 1046-1053.
24. Alexander, A. M., Hargreaves, J. S. J., Mitchell, C. 2013 The denitridation of nitrides of iron, cobalt and rhenium under hydrogen. Topics in Catalysis 56, 1963-1969.

25. McKay, D., Hargreaves, J. S. J., Rico, J. L., Rivera, J. L., Sun, X. L. 2008 The influence of phase and morphology of molybdenum nitrides on ammonia synthesis activity and reduction characteristics. Journal of Solid State Chemistry 181, 325-333.
26. Hargreaves, J. S. J. 2013 Heterogeneous catalysis with metal nitrides. Coordination Chemistry Reviews 257, 2015-2031.
27. Gregory, D. H., Hargreaves, J. S. J., Hunter, S. M. 2011 On the regeneration of Co_3Mo_3N from Co_6Mo_6N with N_2. Catalysis Letters 141, 22-26.
28. Hunter, S. M., McKay, D., Smith, R. J., Hargreaves, J. S. J., Gregory, D. H. 2010 Topotactic nitrogen transfer: Structural transformation in cobalt molybdenum nitrides. Chemistry of Materials 22, 2898-2907.
29. Michalsky, R., Pfromm, P. H. 2011 Chromium as reactant for solar thermochemical synthesis of ammonia from steam, nitrogen, and biomass at atmospheric pressure. Solar Energy 85, 2642-2654.
30. Michalsky, R., Pfromm, P. H. 2012 Thermodynamics of metal reactants for ammonia synthesis from steam, nitrogen and biomass at atmospheric pressure. AIChE Journal 58, 3203-3213.
31. Michalsky, R., Parman, B. J., Amanor-Boadu, V., Pfromm, P. H. 2012 Solar thermochemical production of ammonia from water, air and sunlight: Thermodynamic and economic analyses. Energy 42, 251-260.
32. Michalsky, R., Pfromm, P. H. 2012 An ionicity rationale to design solid phase metal nitride reactants for solar ammonia production. The Journal of Physical Chemistry C 116, 23243-23251.
33. Yang, M. H., Allen, A. J., Nguyen, M. T., Ralston, W. T., MacLeod, M. J., DiSalvo, F. J. 2013 Corrosion behavior of mesoporous transition metal nitrides. Journal of Solid State Chemistry 205, 49-56.
34. Gálvez, M. E., Halmann, M., Steinfeld, A. 2007 Ammonia production via a two-step Al_2O_3/AlN thermochemical cycle. 1. Thermodynamic, environmental, and economic analyses. Industrial & Engineering Chemistry Research 46, 2042-2046.
35. Gálvez, M. E., Frei, A., Halmann, M., Steinfeld, A. 2007 Ammonia production via a two-step Al_2O_3/AlN thermochemical cycle. 2. Kinetic analysis. Industrial & Engineering Chemistry Research 46, 2047-2053.

36. Gálvez, M. E., Hischier, I., Frei, A., Steinfeld, A. 2008 Ammonia production via a two-step Al_2O_3/AlN thermochemical cycle. 3. Influence of the carbon reducing agent and cyclability. Industrial & Engineering Chemistry Research 47, 2231-2237.
37. Oliveira, F. A. C., Rosa, L. G., Peraudeau, G., Granier, B., Fernandes, J. C., Magalhães, T., Shohoji, N. 2012 Crystal grain morphology evolution over Ti, V, Nb and Ta surface heated in N_2 gas environment to 2000 degrees C by filtered concentrated solar beam in a solar furnace at PROMES-CNRS. Materials Transactions 53, 537-545.
38. Bligaard, T., Nørskov, J. K., Dahl, S., Matthiesen, J., Christensen, C. H., Sehested, J. 2004 The Bronsted-Evans-Polanyi relation and the volcano curve in heterogeneous catalysis. Journal of Catalysis 224, 206-217.
39. Barin, I. 1993 Thermochemical Data of Pure Substances, VCH Verlagsgesellschaft mbH, 0-6940 Weinheim, Federal Republic of Germany, ISBN 3-527-28531-8.
40. Michalsky, R., Steinfeld, A., Botu, V., Hargus, C. M., Peterson, A. A. 2014 Design principles for metal oxide redox materials for solar-driven isothermal fuel production. Advanced Energy Materials 4, 1401082 (1-10).
41. Deml, A. M., Stevanović, V., Holder, A. M., Sanders, M., O'Hayre, R., Musgrave, C. B. 2014 Tunable oxygen vacancy formation energetics in the complex perovskite oxide $Sr_xLa_{1-x}Mn_yAl_{1-y}O_3$. Chemistry of Materials 26, 6595-6602.
42. Miller, J. E., McDaniel, A. H., Allendorf, M. D. 2014 Considerations in the design of materials for solar-driven fuel production using metal-oxide thermochemical cycles. Advanced Energy Materials 4, 1300469 (1-19).
43. Faunce, T. A., et al. 2013 Energy and environment policy case for a global project on artificial photosynthesis. Energy & Environmental Science 6, 695-698.
44. Freeman, M. E. (Ed.), Hawkes, S. E. (Ed.), Bennett, B. E. (Ed.), Faunce, T. A., Wasson, A., Crow, K. 2014 Law and global health, Current legal issues, vol. 16, Chapter 26, Environmental sustainability and global health law, The case study of globalizing artificial photosynthesis, Oxford University Press, Oxford, UK.
45. Mortensen, J. J., Hansen, L. B., Jacobsen, K. W. 2005 Real-space grid implementation of the projector augmented wave method. Physical Review B 71, 035109 (1-11).
46. Enkovaara, J., et al. 2010 Electronic structure calculations with GPAW: a real-space implementation of the projector augmented-wave method. Journal of Physics-Condensed Matter 22, 253202 (1-24).

47. Hammer, B., Hansen, L. B., Nørskov, J. K. 1999 Improved adsorption energetics within density-functional theory using revised Perdew-Burke-Ernzerhof functionals. Physical Review B 59, 7413-7421.
48. Bahn, S. R., Jacobsen, K. W. 2002 An object-oriented scripting interface to a legacy electronic structure code. Computing in Science & Engineering 4, 56-66.
49. Both ASE and GPAW are open-source code available from the Department of Physics at the Technical University of Denmark and are available at https://wiki.fysik.dtu.dk/ase/ and https://wiki.fysik.dtu.dk/gpaw/
50. Henkelman, G., Arnaldsson, A., Jónsson, H. 2006 A fast and robust algorithm for Bader decomposition of charge density. Computational Materials Science 36, 354-360.
51. Cairns, A. G., Gallagher, J. G., Hargreaves, J. S. J., McKay, D., Rico, J. L., Wilson, K. 2010 The effect of low levels of dopants upon the formation and properties of beta-phase molybdenum nitride. Journal of Solid State Chemistry 183, 613-619.
52. Liu, Y. J., Xu, L. M., Li, X. Y., Hu, P., Li, S. W. 2010 Growth and magnetic property of ζ-phase $Mn_2N_{1+/-x}$ thin films by plasma-assisted molecular beam epitaxy. Journal of Applied Physics 107, 103914 (1-5).
53. Qiu, C., Guillermet, A. F. 1993 Predicative approach to the entropy of manganese nitrides and calculation of the Mn-N phase-diagram. Zeitschrift für Metallkunde 84, 11-22.
54. Yang, M. H., MacLeod, M. J., Tessier, F., DiSalvo, F. J. 2012 Mesoporous metal nitride materials prepared from bulk oxides. Journal of the American Ceramic Society 95, 3084-3089.
55. Furler, P., Scheffe, J., Marxer, D., Gorbar, M., Bonk, A., Vogt, U., Steinfeld, A. 2014 Thermochemical CO_2 splitting via redox cycling of ceria reticulated foam structures with dual-scale porosities. Physical Chemistry Chemical Physics 16, 10503-10511.
56. Venstrom, L. J., De Smith, R. M., Hao, Y., Haile, S. M., Davidson, J. H. 2014 Efficient splitting of CO_2 in an isothermal redox cycle based on ceria. Energy & Fuels 28, 2732-2742.
57. Zhang, J.-Z., Xu, C.-S., Zhao, Y.-P. 2008 Kinetics of nitrogen diffusion in granular manganese. Journal of Iron and Steel Research International 15, 85-88.
58. Jauberteau, I., Jauberteau, J. L., Goudeau, P., Soulestin, B., Marteau, M., Cahoreau, M., Aubreton, J. 2009 Investigations on a nitriding process of molybdenum thin films exposed to (Ar-N_2-H_2) expanding microwave plasma. Surface & Coatings Technology 203, 1127-1132.

59. Mändl, S., Manova, D., Gerlach, J. W., Assmann, W., Neumann, H., Rauschenbach, B. 2004 High temperature nitrogen plasma immersion ion implantation into molybdenum. Surface & Coatings Technology 180, 362-366.
60. Valov, I., et al. 2009 Ionic and electronic conductivity of nitrogen-doped YSZ single crystals. Solid State Ionics 180, 1463-1470.
61. Skúlason, E., Bligaard, T., Gudmundsdóttir, S., Studt, F., Rossmeisl, J., Abild-Pedersen, F., Vegge, T., Jónsson, H., Nørskov, J. K. 2012 A theoretical evaluation of possible transition metal electro-catalysts for N_2 reduction. Physical Chemistry Chemical Physics 14, 1235-1245.
62. Hammer, B., Nørskov, J. K. 1995 Electronic factors determining the reactivity of metal surfaces. Surface Science 343, 211-220.

Figure captions

Figure 1: Solar-driven low-pressure ammonia synthesis with (A) manganese nitride and (B) molybdenum nitride redox materials, shown schematically with panel (C). Negative values (shaded regions) of the thermodynamic equilibria indicate exergonic reactions; pH_2O is fixed at 1.5 x 10^{-4} bar for the reduction of MnO, while pCO_2 is fixed at 4.0 x 10^{-1} bar for the reduction of MoO_2. Online version in colour.

Figure 2: Designing metal nitride redox materials: Free energy of the nitrogen vacancy formation in $D_{0.25}Mn_{1.75}N$ metal nitrides doped with a transition metal, D (marked) vs. the number of electrons in the dopant d-states. The solid line marks ΔG_v[N] for Mn_2N; the dashed line is a linear regression (R^2 ~ 0.75). The filled symbol marks a system that is studied experimentally in this work. Online version in colour.

Figure 3: Designing metal nitride redox materials: Free energy of the nitrogen vacancy formation in $D_{0.5}Mo_{1.5}N$ metal nitrides doped with a transition metal, D (marked) vs. the number of electrons in the dopant d-states. The solid line marks ΔG_v[N] for Mo_2N; the dashed line is a linear regression (R^2 ~ 0.93). The filled symbol marks a system that is studied experimentally in this work. Online version in colour.

Figure 4: Kinetics of the N_2 reduction: Reaction yield in mol% of the indicated metal nitride formed relative to a stoichiometric conversion of Mn at 750°C with (A) Mn and (B) Fe-doped Mn forming Mn_4N (light orange symbols) and $Mn_6N_{2.58}$ (dark blue symbols). Error propagation within a 95% confidence interval (error bars) yields in average ±17.81%. Solid lines are kinetic models limited by solid-state diffusion that are fitted to the data at 5-30 min for Mn_4N and 60-240 min for $Mn_6N_{2.58}$. Online version in colour.

Figure 5: Kinetics of the N_2 reduction: Reaction yield in mol% $FeN_{0.0324}$ formed relative to a stoichiometric conversion of Fe at 750°C with pure Fe (circles) and Fe-doped Mn (triangles). Error propagation within a 95% confidence interval (error bars) yields in average ± 20.83%. The solid line is a kinetic model limited by solid-state diffusion that is fitted to the data at 60-240 min. Online version in colour.

Figure 6: Scanning electron micrographs for (A) Mn_4N and (B) Mo/Mo_2N, and (C) Energy-dispersive X-ray spectroscopy analysis of mostly Cr_2N (mixed blue/red domains) and Mo (green domains) formed from an equimolar mixture of Mo (green signal) and Cr (blue signal) powder after nitridation for 2 hrs at 750°C in N_2 (red signal). Online version in colour.

Figure 7: Electronic structure analysis: (A) Dopant-projected density of states (DOS) of $D_{0.5}Mo_{1.5}N_{0.5}$ bulk for the marked representative dopants D (occupied states below the Fermi level are shaded and the position of the d-band center is indicated with a dashed line), and correlations of the free energy of the nitrogen vacancy formation with (B) the d-band center and (C) the s- and p-band centers of $D_{0.5}Mo_{1.5}N_{0.5}$. The complete data is provided with SI. Solid lines are linear regressions to the data shown with filled symbols. Online version in colour.

Figure 8: Correlations of the free energy of the nitrogen vacancy formation with the partial average charge of the (A) dopant and (B) lattice nitrogen. Solid lines are linear regressions to the data shown with filled symbols. The data with the highest and lowest partial charges are marked with the dopant. Empty symbols are the un-doped metal nitrides (marked with the metallic constituent) and metal nitrides doped with Zn (marked with Zn). All data is given with SI. Online version in colour.

Figure 9: (A) Charge density differences (in units of the elementary charge per $Å^3$) due to the formation of nitrogen vacancies in $D_{0.5}Mo_{1.5}N$ (shown at the height of the nitrogen nucleus). The first panel in the first row is a schematic of the metal nitride crystal geometry with solid and dashed circles marking atoms in the upper and lower plane of the bulk models, respectively. (B) A schematic of the correlation between the nitrogen binding strength and the charge density and location near the nitrogen vacancy. M, V, and D mark the parent metal, the nitrogen vacancy, and the dopant, while a bold (simple) "+" or "-" mark the strong (weak) accumulation of positive or negative charge, respectively. Online version in colour.

Supporting Information for:

Rational design of metal nitride redox materials for solar-driven ammonia synthesis

Ronald Michalsky[1, *], Peter H. Pfromm[2], Aldo Steinfeld[1]

[1] Department of Mechanical and Process Engineering, ETH Zürich, 8092 Zürich, Switzerland, [2] Department of Chemical Engineering, 1005 Durland Hall, Kansas State University, Manhattan, KS, 66506, U.S.A.

Corresponding Author

[*] Present address: ETH Zürich, Institute of Energy Technology, Sonneggstrasse 3, ML K 23, 8092 Zürich, Switzerland; E-mail: michalskyr@ethz.ch; Telephone: +41-44-6338383

Keywords

Renewable energy, Concentrated solar energy, Thermochemical redox cycle, Hydrogen storage, Haber Bosch, Density functional theory

Overview

1. Stoichiometry of the redox cycle

The reaction stoichiometry of the solar thermochemical ammonia synthesis via a two-step redox cycle can be represented with:

Metal nitride oxidation (Ammonia evolution):

$$\frac{1}{b}M_aN_b + \frac{ad}{bc}H_2O \rightarrow \frac{a}{bc}M_cO_d + NH_3 + \left(\frac{ad}{bc} - \frac{3}{2}\right)H_2 \quad \text{(S1)}$$

Metal oxide reduction (Nitrogen reduction):

$$\frac{a}{bc}M_cO_d + \frac{1}{2}N_2 \rightarrow \frac{1}{b}M_aN_b + \frac{ad}{2bc}O_2 \quad \text{(S2)}$$

where M denotes a metal and M_aN_b and M_cO_d are the (completely) nitrated and oxidized forms of the metal nitride redox material with generalized stoichiometry. We note the thermochemical equilibrium of the metal oxide reduction can be shifted towards the formation of the reaction products via adjusting the process pressure and temperature and via coupling the reaction to the oxidation of a chemical reducing agent such as CO, H_2, or gasified biomass.

2. Computational details

2.1 Thermochemical equilibrium calculations

Thermochemical data [1] were extrapolated for Mn_4N at ≥ 700 K (R^2 = 1), for Mn_5N_2 at ≥ 900 K (R^2 = 0.999999), and for Mo_2N at ≥ 1500 K (R^2 = 0.999997) using third-order polynominal regressions.

2.2 Local optimization procedures

In all DFT calculations the linesearch BFGS algorithm was employed to optimize the atomic geometries until the maximum force was less than 0.05 eV $Å^{-1}$. Convergence was achieved with a Fermi-Dirac smearing of 0.1 eV and the structure optimization results were extrapolated to 0 K. The lattice constants of the Mo_2N and Mn_2N bulk metal nitrides were chosen as the DFT-calculated bulk lattice constants to avoid reminiscent stress in the calculations. We note, the DFT-computed lattice constants (i.e., a = 4.220 Å for Mo_2N and a = 2.853 Å and c = 4.393 Å for Mn_2N) compare well with the experimental values (i.e., a = 4.163 Å for Mo_2N [2] and a = 2.844 Å and c = 4.509 Å or Mn_2N [3]), which is a relative difference of 0.32-2.57% that is within the uncertainty of DFT calculations. [4],[5]

2.3 Free energy computations

The free energies of the chemical species i (G_i) was calculated with: [5]

$$G_i(T,P) = N_i\mu_i(T,P) = E_i + U_{ZPE,i} - TS_i(T,P) \quad \text{(S3)}$$

where T is the absolute temperature (298.15 K), P is the absolute pressure (1.013 bar), N_i is the number of atoms, μ_i is the chemical potential, E_i is the DFT-determined total electronic energy, $U_{ZPE,i}$ is the zero-point vibrational energy, and S_i is the entropy. N_2 was assumed to be an ideal gas, while the liberated lattice nitrogen was computed based on the harmonic approximation where all degrees of freedom are treated as frustrated harmonic vibrations and pressure-volume contributions are neglected. All thermodynamic properties were calculated from vibrational frequencies and standard statistical mechanical equations, evaluated through ASE, and free energy corrections of the solids were neglected. [6]

The free energy of forming nitrogen vacancies (ΔG_v[N]) in the bulk was computed with: [7]

(S4) $$\Delta G_v[\mathrm{N}] = G_v - (G_s - G_\mathrm{N}^r)$$

where G_v, G_s and G_N^r are the free energies of the metal nitride model with the nitrogen vacancies, the stoichiometric metal nitride (without nitrogen vacancies) and the reference energy of the lattice nitrogen yielding N_2 gas. Negative free energies indicate an exergonic evolution of the lattice nitrogen. The reference free energy of nitrogen (G_N^r) is computed from stable N_2 gas, [4],[5] with:

(S5) $$G_\mathrm{N}^r = G[\mathrm{N}_2]/2$$

where $G[N_2]$ is the free energy of N_2 molecules in the gas phase.

2.4 Charge density differences

The charge density difference (CDD) for doping a metal nitride is computed as the difference between the volumetric charge density (CD) of a doped bulk metal nitride and the CD of the metal nitride without the dopant. Analogously, the CDD for the formation of nitrogen vacancies is computed as the CD of a metal nitride model with nitrogen vacancies plus the CD of the balance of atomic nitrogen minus the CD of the stoichiometric metal nitride model.

3. Experimental details

3.1 N_2 reduction

The level of impurities of the metal precursors is given by the manufacturer (Noah Technologies) for Mn (99.9% pure) with: 0.0015% Ag, 0.0030% Al, 4.16 ppm As, 3.78 ppm B, < 1 ppm Ba, < 1 ppm Be, < 1 ppm Bi, 0.0099% Ca, < 1 ppm Cd, 2.38 ppm Co, 0.0059% Cr, < 1 ppm Cu, 0.0571% Fe, < 8 ppm K, 3.19 ppm La, < 1 ppm Li, < 4 ppm Mg, < 1 ppm Mo, < 0.001% Na, < 1 ppm Ni, < 4 ppm P, 0.0019% Pb, < 4 ppm Pd, 0.0379% S, 0.0020% Sb, 0.0076% Se, 0.0070% Si, < 4 ppm Sn, < 1 ppm Sr, < 4 ppm Th, < 2 ppm Ti, 0.0177% Tl, < 0.002 % U, < 1 ppm V, 9.73 ppm W, < 1 ppm Y, < 1 ppm Zn, < 2 ppm Zr; for Mo (99.95% pure) with: < 1 ppm Al, < 1 ppm Co, < 1 ppm Cr, < 1 ppm Cu, < 1 ppm Fe, < 1 ppm Mg, < 1 ppm Mn, < 1 ppm Ni, < 0.004% W, < 0.015% O_2, < 0.001% C (total); for Fe (99.9% pure) with: < 3 ppm As, < 2 ppm Hg, < 4 ppm Pb, 0.04% acid insolubles; and for Cr (99.8% pure) with: 0.10% Fe, 0.012% C, 0.68% O, 0.022% S.

Table S1 summarizes the characterization of the metal reactants and the metal nitrides that were formed from pure metal powder and N_2. We note Table S1 does not list the discussed cubic $FeN_{0.0324}$ since this compound was not obtained with pure Fe powder.

Table S1: Characterization of the metal and binary metal nitride powder beds

metal	Mo	Cr	Fe	Mn	nitride	β-Mo_2N	Cr_2N (CrN)	ε-Mn_4N (ζ-$Mn_6N_{2.58}$)
space group [A]	$Im\bar{3}m$	$Im\bar{3}m$	$Im\bar{3}m$	$I4\bar{3}m$		$I4_1/amd$	$P\bar{3}1m$ ($Fm\bar{3}m$)	$Pm\bar{3}m$ ($P6_322$)
d_p [B] (μm)	6 ± 4	18 ± 13	29 ± 21	43 ± 22		7 ± 4	17 ± 11	46 ± 19
A_{BET} [C] (m^2 kg^{-1})	429 ± 3	692 ± 8	281 ± 5	269 ± 2		426 ± 3	654 ± 9	270 ± 3
Φ [D] (m^3 m^{-3})	0.75	0.57	0.66	0.62		-	-	-

[A]) via X-ray diffraction; [B]) average particle diameter; [C]) BET surface area; [D]) void space fraction $\Phi = 1 - \rho_{bulk}/\rho_{particle}$, where ρ_i is the density in kg m^{-3}, relative error via error propagation ± 5.98 %; generally, powder bed surface = 33 ± 2 cm^2, powder bed thickness < 1 mm.

The tube furnace employed in this work was equipped with a quartz tube (60 mm inner diameter, 1 m length) that was purged for 10 min with 0.5-0.9 $L_{(STP)}$ N_2 min^{-1} before each experiment. The heating rate (r_h) for N_2 reduction experiments at 750°C was approximately $r_h = At + B$, where t is the heating time in min, A = -6.91 °C min^{-2} and B = 77.4 °C min^{-1}.

To determine the temperature that results in a minimum formation of surface oxides during the nitridation of Mo, the reaction of Mo powder with N_2 was studied at various reaction temperatures hold for 2 hrs: 998 ± 3 mg Mo was placed into a quartz boat, pretreated for 10 min at 60°C to remove water, and thereafter introduced into the tube furnace at 400°C and heated to 450, 500, 550, 600, 650, 700, 750, 1000 and 1200°C respectively. Heating was approximately linear with A in the range of -9.36 to -2.82 °C min^{-2} (for maximum temperatures in the range of 1200 to 450°C) and B in the range of 65.9 to 67.9 °C min^{-1} (for maximum temperatures in the range of 450 to 1200°C). H_2 was supplied at 0.47 ± 0.05 $L_{(STP)}H_2$ min^{-1} and replaced with a flow of 1.86 ± 0.05 $l_{(STP)}N_2$ min^{-1} when the maximum reaction temperature was reached. After 2 hrs the furnace was cooled (at about -13.5 to -2.73 °C s^{-1} within the first 60 s, -3.85 to 0.767 °C s^{-1} at 60 to 180 s and above -0.767 °C s^{-1} at above 180 s) to below 75°C. The solid was removed and stored under air at 4°C. To eliminate the possibility of rapid quenching affecting the yield of Mo_2N, the nitridation of Mo for 2 hrs with N_2 at 450 or 750 °C was repeated with a cooling rate of about -6.05 to -1.80 °C min^{-1}. This decrease in the cooling rate did not affect the Mo_2N yield.

3.2 Processing of experimental data

The yield (X_i) of the chemical species j (a metal, metal nitride or metal oxide, respectively) is reported as the molar ratio of a chemical species detected after the experiment (n_j in mol) relative to the theoretical amount of that species formed at stoichiometric conversion of the metal reactant (n_j^* in mol)

$$X_j = \frac{n_j}{n_j^*} = \frac{\Delta m_t x_j M_{metal}}{\Delta m_0 x_{metal} M_j a_j} \quad \text{(S6)}$$

where Δm (in g) is the mass difference between the solid reactant and the quartz boat at time t and before the reaction (subscript 0), x (in g g^{-1}) is the metal, metal nitride, or metal oxide weight fraction, M (in g mol^{-1}) is the molar mass, and a is a dimensionless coefficient that is accounting for the stoichiometric amount of metal atoms contained in the reaction product.

To assess the effect of solid-state diffusion limitations, a diffusion-limited shrinking-core model for spherical particles with constant size [8] was applied to the experimental data:

$$kt = 1 - 3 \times (1 - X_j)^{2/3} + 2 \times (1 - X_j) \quad \text{(S7)}$$

where k (in s^{-1}) is a specific rate constant. We note this model describes the reported kinetic data best (highest R^2) when compared to kinetic models that account for limiting gas phase diffusion or available surface area. [8]

4. Supporting results

4.1 N_2 reduction with Mo, Cr, and Cr-doped Mo

Figure S1 shows the formation of Mo_2N and MoO_2 from Mo heated in N_2. XRD showed formation of tetragonal β-Mo_2N with a homogeneity range of 28.7 to 34.5 mol% N. Thus, quantitative calculations in this work assume stoichiometric Mo_2N as-indicated. Given the minimum MoO_2 yield and maximized Mo_2N near this temperature, Mo was nitrated at 750°C in this work.

Figure S2 shows the formation of Mo_2N with pure Mo powder or Cr-doped Mo powder and N_2 or a mixture of H_2 and N_2; the formation of Cr_2N and CrN with pure Cr powder and N_2 or a mixture of H_2 and N_2 is shown for reference. The nitridation of Mo at 750°C and 1 bar reaches a 1.2 mol% yield after 0.5 min, that is increasing thereafter with diminished kinetics to a maximum of 3.3 mol% after 120 min. Cr fixes N_2 quickly forming 66 ± 3 mol% Cr_2N after 10 min, which converts into up to 15.8 ± 0.5 mol% CrN after 120 min. The formation of CrN is slow and is described well with a diffusion-limited reaction mechanism ($R^2 > 0.94$). Forming the nitrides in presence of H_2 affects the yield of Cr_2N and CrN only slightly but increased the yield of Mo_2N more than six-fold to 21.1 ± 0.7 mol% after 120 min. While the formation of the trigonal Cr_2O_3 phase was in average 34% below the yield of Cr_2O_3 when reacting the metal with N_2 only (which yielded 0 to 2.7 mol% Cr_2O_3), MoO_2 or MoO_3 were not detected. The yield of Mo_2N from Mo/Cr powder mixtures reacted with N_2 or the N_2/H_2 gas mixture differs only slightly from the results obtained with Mo and the N_2/H_2 gas mixture; in presence of Cr after 120 min 18 ± 2 and 23 ± 5 mol% Mo_2N were formed in absence or presence of H_2, respectively. The limited yield of Mo_2N from Mo and N_2 that is increased by the presence of H_2 or Cr can be understood due to the reduction of a thin layer MoO_2 that limits the formation of Mo_2N at the surface of the Mo reactant, yielding H_2O or traces of chromium oxides with H_2 or Cr respectively. The generally slow formation of Mo_2N in presence of Cr or H_2 indicates that the hypothesized promotion of the N_2 reduction yield with Mo by the presence of Cr cannot be assessed due to diffusion limitations that prevent reaching the thermochemical equilibrium at the studied experimental conditions.

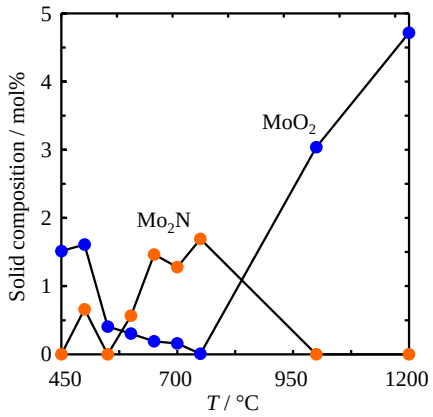

Figure S1: Formation of Mo_2N (light orange symbols) or MoO_2 (dark blue symbols) in mol% of the indicated metal compound formed relative to stoichiometric conversion of Mo after heating at a given temperature for 2 hrs with 1 bar N_2. Lines are a guide only. The average relative error of the data within a 95% confidence interval is ± 22.86%.

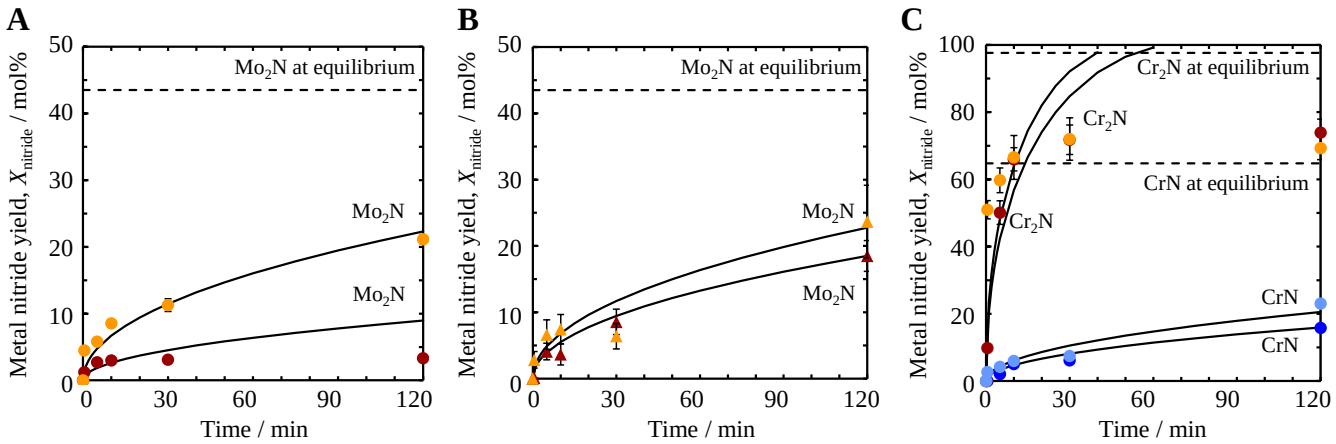

Figure S2: Reduction of N_2 at 750°C with (A) Mo and 1 bar N_2 (dark red symbols) or 0.199 bar H_2 diluted in 0.801 bar N_2 (light orange symbols) forming Mo_2N, (B) an equimolar mixture of Mo and Cr and 1 bar N_2 (dark red symbols) or 0.199 bar H_2 diluted in 0.801 bar N_2 (light orange symbols) forming Mo_2N, and (C) Cr and 1 bar N_2 forming Cr_2N (dark red symbols) and CrN (dark blue symbols) or 0.199 bar H_2 diluted in 0.801 bar N_2 forming Cr_2N (light orange symbols) and CrN (light blue symbols). Error bars are via error propagation within a 95% confidence interval. Solid lines are kinetic models limited by solid-state diffusion that are fitted to the data at 0.5-120 min. Dashed lines are the approximate location of the thermodynamic equilibrium for forming the indicated metal nitride with N_2.

Figure S3 shows the morphology of Mo as-purchased, after heating in N_2, and after heating in H_2/N_2. The analysis shows while Mo retains its hexoctahedral symmetry after heating with N_2 it is apparently covered with a structure that replaces the terrace-like appearance of the pristine Mo surface. Heating Mo in H_2/N_2 results in the disappearance of the hexoctahedral symmetry of Mo. This in conjunction with the increased yield of Mo_2N when heating Mo in H_2/N_2 confirms the interpretation that MoO_2 is formed from traces O_2 and H_2O at the surface of Mo that is heated in N_2. This oxide layer limits the formation of Mo_2N. The oxide layer is removed in the presence of H_2 which explains the increased yield of Mo_2N due to decreased diffusion limitations.

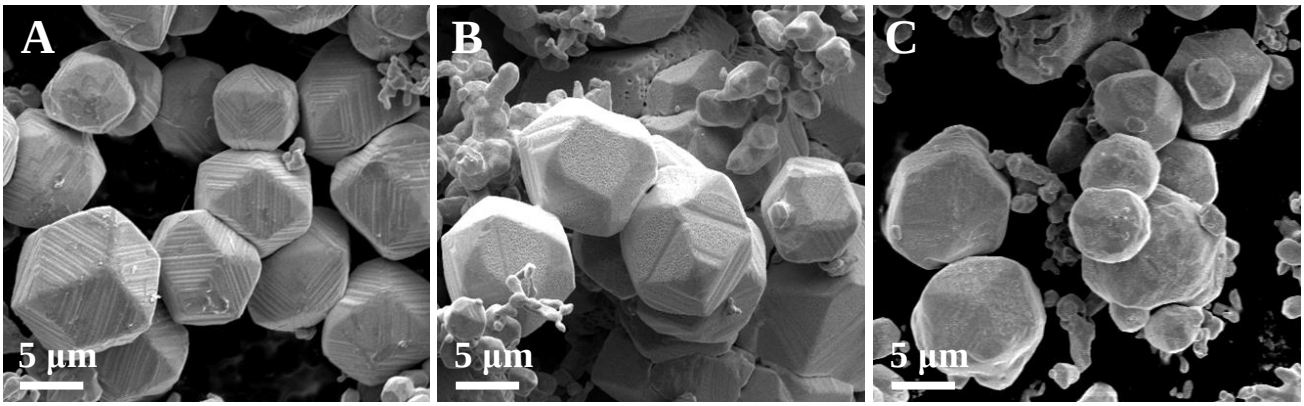

Figure S3: Scanning electron micrographs of Mo samples (A) as-purchased, (B) after heating for 2 hrs at 750°C in N_2, or (C) in 0.199 bar H_2 diluted in 0.801 bar N_2.

Table S2 summarizes the reaction rate constants determined from the experimental data and shrinking-core models that account for solid-state diffusion limitations.

Table S2: Reaction rate constants, k

Solid reactant [A]	Solid product	Gas phase [B]	Time range / s	k / s^{-1}
Mn	Mn_4N	N_2	5-30	4.14×10^{-4}
Mn	$Mn_6N_{2.58}$	N_2	60-240	3.71×10^{-5}
Mn/Fe	Mn_4N	N_2	5-30	1.81×10^{-4}
Mn/Fe	$Mn_6N_{2.58}$	N_2	60-240	3.89×10^{-6}
Mn/Fe	$FeN_{0.0324}$	N_2	60-240	1.20×10^{-5}
Mo	Mo_2N	N_2	5-120	3.88×10^{-7}
Mo	Mo_2N	N_2/H_2	5-120	2.57×10^{-6}
Mo/Cr	Mo_2N	N_2	5-120	1.73×10^{-6}
Mo/Cr	Mo_2N	N_2/H_2	5-120	2.68×10^{-6}
Cr	Cr_2N	N_2	5-120	2.49×10^{-4}
Cr	Cr_2N	N_2/H_2	5-120	3.37×10^{-4}
Cr	CrN	N_2	5-120	1.27×10^{-6}
Cr	CrN	N_2/H_2	5-120	2.15×10^{-6}

[A]) pure or equimolar mixtures; [B]) 1 bar N_2 or 0.199 bar H_2 diluted in 0.801 bar N_2

From the experimental data an apparent diffusion constant, D, can be estimated with [8]:

$$D = \frac{\rho_p d_p^2 k}{24 b c_g} \quad \text{(S8)}$$

where ρ_p (in mol m^{-3}) is the density of the solid reactant, d_p (in m) is the average particle diameter, b is the dimensionless molar ratio of reacted solid per reacted N_2, and c_g (in mol m^{-3}) is the molar concentration of N_2. The computation was limited to the reported kinetic data that is well described with equation S7 (i.e., R^2 in the range of 0.90 to 0.98 for CrN and Mo_2N respectively, 0.80 to 0.85 for $Mn_6N_{2.58}$).

Figure S4 plots D vs. the theoretical volume fraction, f_v, occupied by atoms or ions:

(S9) $$f_v = \frac{4\pi N_A \rho}{3} \sum_{k=\text{all constituents}} \gamma_k r_k^3$$

where N_A is Avogadro's constant, ρ (in mol m^{-3}) is the molar density of the formed reaction product, γ_k is the dimensionless fraction of atoms per product phase, and r_k (in m) is the radius of the nitrogen or the metallic constituent of the metal nitride. Based on the relative low electronegativity of Mn, nominal N^{3-} ions were assumed for $Mn_6N_{2.58}$ (i.e., Mn in 2+ oxidation state). CrN and Mo_2N [9],[10] were computed as metallic compounds (i.e., atomic N bonded covalently by 12-coordinated metal atoms). MoO_2 that is presumably present when reacting Mo with N_2 was included as ideal ionic compound.

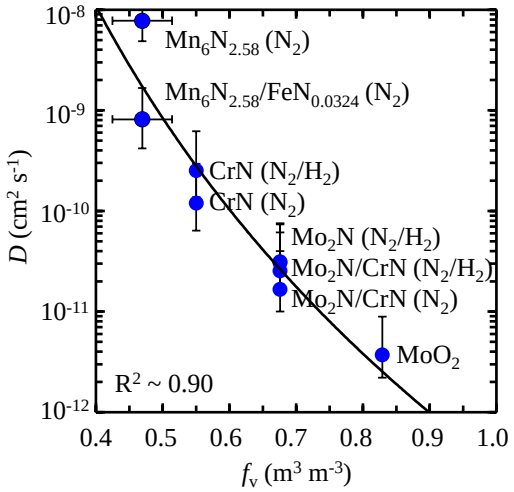

Figure S4: Apparent diffusion coefficients for the diffusion through the marked solid at 750°C vs. the theoretical volume occupied by metal and nitrogen or oxygen atoms. The density of $Mn_6N_{2.58}$ was estimated with 6,131 ± 292 kg m^{-3}. The solid line is to guide the eye. Error propagation within a 95% confidence (error bars) yields in average ± 17.81%. The highest present nitride phases are indicated along with the gases present during the nitridation experiments in parenthesis.

4.2 Electronic structure details

Table S3 summarizes the Bader charge analysis of the metal nitrides models.

Table S3: Partial charges, q_{Atom} / e

Atom	D in $D_{0.25}Mn_{1.75}N$										
	Sc	Ti	V	Cr	Mo	Mn	Fe	Co	Ni	Cu	Zn
D	1.4743	1.4072	1.1414	0.8612	0.8437	0.7359	0.5704	0.3954	0.2978	0.3484	0.5600
Mn	0.6244	0.6565	0.6959	0.7185	0.7275	0.7359	0.7601	0.7863	0.7972	0.7820	0.7493
Mn	0.7879	0.7587	0.7363	0.7199	0.7750	0.7375	0.7318	0.7187	0.7249	0.7363	0.8200
Mn	0.6383	0.6606	0.7002	0.7384	0.7048	0.7374	0.7509	0.7689	0.7693	0.7628	0.7423
Mn	0.5855	0.6081	0.6727	0.7144	0.7405	0.7375	0.7686	0.7930	0.8037	0.7828	0.7542
Mn	0.6383	0.6606	0.7000	0.7385	0.7049	0.7374	0.7509	0.7689	0.7693	0.7626	0.7423
Mn	0.6244	0.6564	0.6957	0.7189	0.7275	0.7359	0.7603	0.7861	0.7971	0.7818	0.7496
Mn	0.6319	0.6526	0.6914	0.7300	0.6938	0.7359	0.7497	0.7693	0.7808	0.7813	0.7487
N	-1.5097	-1.5302	-1.5196	-1.4896	-1.4866	-1.4734	-1.4562	-1.4346	-1.4204	-1.4186	-1.4663
N	-1.5093	-1.5279	-1.5204	-1.4882	-1.4850	-1.4735	-1.4550	-1.4358	-1.4198	-1.4195	-1.4644
N	-1.5093	-1.5279	-1.5194	-1.4884	-1.4850	-1.4734	-1.4549	-1.4357	-1.4198	-1.4197	-1.4644
N	-1.4767	-1.4747	-1.4745	-1.4738	-1.4612	-1.4734	-1.4766	-1.4807	-1.4803	-1.4805	-1.4715
Atom	D in $D_{0.5}Mo_{1.5}N$										
	Sc	Ti	V	Cr	Mo	Mn	Fe	Co	Ni	Cu	Zn
D	1.5287	1.4596	1.1713	0.8630	1.0437	0.6739	0.5582	0.4385	0.4304	0.4793	0.8033
Mo	1.0475	1.0703	1.0988	1.1305	1.0435	1.1513	1.1715	1.1861	1.1754	1.1651	1.1265
Mo	0.3489	0.3987	0.4934	0.5736	0.5654	0.6160	0.6499	0.6660	0.6646	0.6347	0.5663
Mo	0.3493	0.3989	0.4936	0.5739	0.5654	0.6157	0.6505	0.6659	0.6646	0.6350	0.5664
N	-1.6383	-1.6649	-1.6298	-1.5717	-1.6102	-1.5292	-1.5164	-1.4795	-1.4686	-1.4584	-1.5325
N	-1.6384	-1.6650	-1.6297	-1.5717	-1.6104	-1.5301	-1.5160	-1.4794	-1.4688	-1.4582	-1.5325

Figure S5 shows a complete density of states (DOS) analysis of the dopant-projected d-states. The figure shows how the dopant d-states are increasingly occupied when moving the dopant in the periodic table from the left to the right, which is shown in the manuscript representatively for $Ti_{0.5}Mo_{1.5}N$, $Mo_2N_{0.5}$, and $Cu_{0.5}Mo_{1.5}N_{0.5}$. Furthermore, the figure shows how the deviation of Zn-doped compounds from the correlations discussed in the manuscript can be understood due to the energetically highly stable and essentially fully occupied d-states of the Zn dopant, when compared to the DOS of all other dopants in both Mo_2N- and Mn_2N-based metal nitrides.

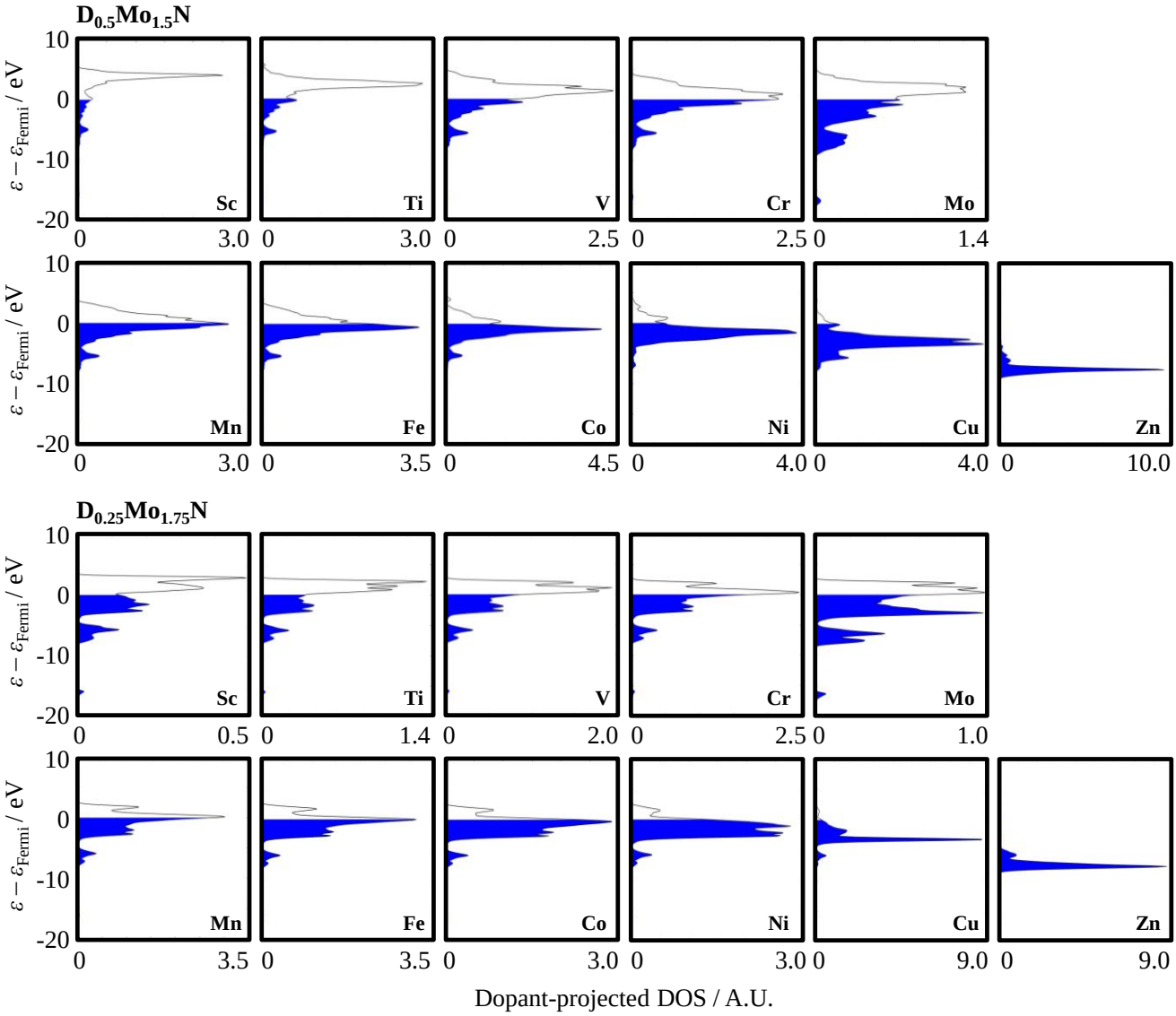

Figure S5: Density of states (DOS) for stoichiometric $D_{0.5}Mo_{1.5}N$ (using a **k**-point sampling of 12×12×12, except 8×8×8 for D = Ni) and $D_{0.25}Mn_{1.75}N$ (using a **k**-point sampling of 8×8×8); the dopant, D, is marked on each DOS plot and the occupied states below the Fermi level are shaded in blue.

Comparable to the trends in the quantity of the charge density transfer, doping transition-metal nitrides with different metals shows as well trends in the geometry of the charge redistribution. Figure S6 shows the difference in the volumetric charge density between doped Mn_2N and un-doped Mn_2N. Darker shaded areas mark regions with accumulated charge (charge sinks) while lighter areas mark regions from which charge is withdrawn (charge sources). Comparing the charge density differences at the height of the dopant nucleus across the tested dopants shows a polarization of the charge density difference near the dopant with a distinct charge source that is opposite to a charge sink for all dopants with fewer or equal valence electrons in d-orbitals, relative to the Mn $3d^5$ occupancy (i.e., Sc to Cr and Mo). In these materials the nitrogen vacancies are formed at the lattice nitrogen that is marked with a solid circle in the schematic of the crystal geometry. With decreasing stability of the lattice nitrogen due to doping with metals

that have more valence electrons in d-orbitals relative to Mn (i.e., Fe to Zn), this polarization of the charge density difference rotates by about 180°. For the Fe, Co and Ni dopants, this coincides with the formation of the nitrogen vacancies at the lattice nitrogen that is marked with a dashed circle, i.e., along an axis that is rotated by 180° relative to the vacancy formation in the metal nitrides with a reversed polarization of the charge density difference. For the two dopants with nearly or completely filled d-states, i.e., Cu and Zn, the nitrogen vacancies are formed at the lattice nitrogen that is marked with a solid circle.

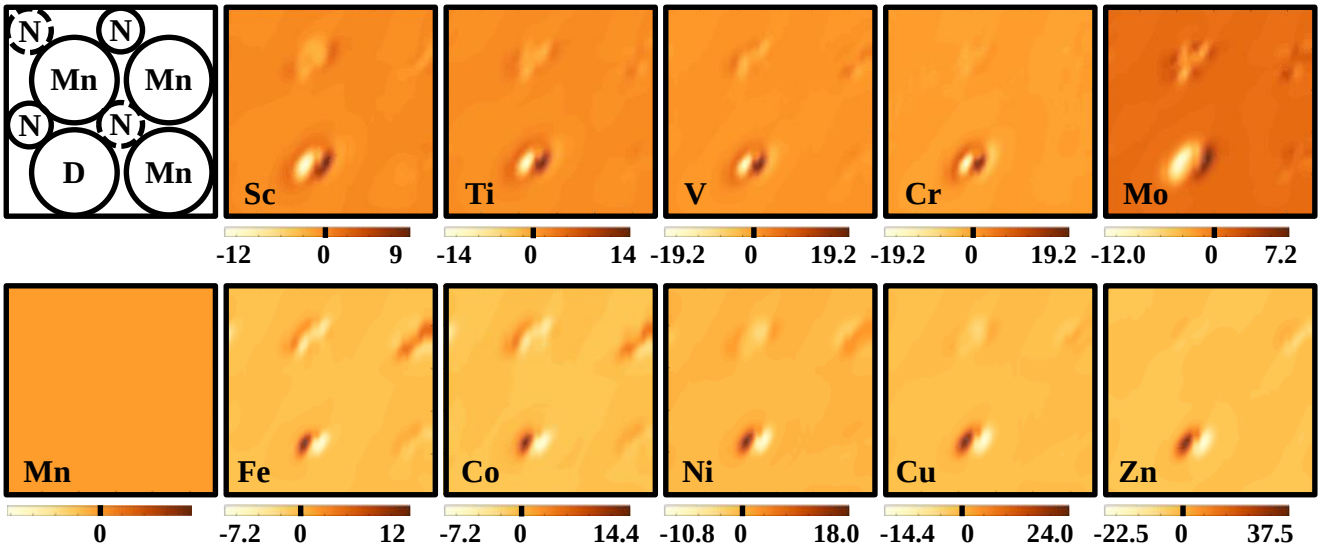

Figure S6: Charge density differences (in units of the elementary charge per Å^3) due to doping $D_{0.25}Mn_{1.75}N$ bulk with the indicated dopant D (shown at the height of the dopant nucleus). The first panel in the first row is a schematic of the metal nitride crystal geometry with solid and dashed circles marking atoms in the upper and lower plane of the bulk models, respectively.

5. References

1. Barin, I., Thermochemical Data of Pure Substances, VCH Verlagsgesellschaft mbH, 0-6940 Weinheim, Federal Republic of Germany, 1993.

2. Gouin, X., et al., Reaction of ammonia with molybdenum oxide - physicochemical characterization of an Mo_2N-gamma type oxynitride phase. Journal of Solid State Chemistry, 1994. 109(1): p. 175-180.

3. Liu, Y.J., et al., Growth and magnetic property of ζ-phase $Mn_2N_{1+/-x}$ thin films by plasma-assisted molecular beam epitaxy. Journal of Applied Physics, 2010. 107(10): p. 103914 (1-5).

4. Michalsky, R., et al., Departures from the adsorption energy scaling relations for metal carbide catalysts. Journal of Physical Chemistry C, 2014. 118: p. 13026-13034.

5. Medford, A.J., et al., Elementary steps of syngas reactions on Mo_2C(001): Adsorption thermochemistry and bond dissociation. Journal of Catalysis, 2012. 290: p. 108-117.

6. Zeng, Z.H., et al., Generalized trends in the formation energies of perovskite oxides. Physical Chemistry Chemical Physics, 2013. 15(20): p. 7526-7533.

7. Michalsky, R., et al., Design principles for metal oxide redox materials for solar-driven isothermal fuel production. submitted to Advanced Energy Materials, 2014.

8. Levenspiel, O., Chemical reaction engineering, Third Edition, Chapter 25 Fluid-particle reactions: Kinetics. New York: John Wiley & Sons, 1999.

9. Chen, H., et al., Structures and electronic properties of $Mo_{2n}N_n$ (n=1-5): a density functional study. Chinese Physics B, 2010. 19(12): p. 123601-1 - 123601-11.

10. Qi, J., et al., Theoretical and experimental studies on the relationship between the structures of molybdenum nitrides and their catalytic activities toward the oxygen reduction reaction. Journal of Physical Chemistry C, 2010. 114(42): p. 18159-18166.